Rambutan-Like FeCO$_3$ Hollow Microspheres: Facile Preparation and Superior Lithium Storage Performances

Yiren Zhong, Liwei Su, Mei Yang, Jinping Wei, and Zhen Zhou*

Tianjin Key Laboratory of Metal and Molecule Based Material Chemistry, Key Laboratory of Advanced Energy Materials Chemistry (Ministry of Education), Institute of New Energy Material Chemistry, Synergetic Innovation Center of Chemical Science and Engineering (Tianjin), Nankai University, Tianjin 300071, People's Republic of China

S *Supporting Information*

ABSTRACT: Rambutan-like FeCO$_3$ hollow microspheres were prepared via a facile and economic one-step hydrothermal method. The structure and morphology evolution mechanism was disclosed through time-dependent experiments. After undergoing the symmetric inside-out Ostwald ripening, the resultants formed microporous/nanoporous constructions composed of numerous one-dimensional (1D) nanofiber building blocks. Tested as anode materials of Li-ion batteries, FeCO$_3$ hollow microspheres presented attractive electrochemical performances. The capacities were over 1000 mAh g^{-1} for initial charge, ~880 mAh g^{-1} after 100 cycles at 50 mA g^{-1}, and ~710 mAh g^{-1} after 200 cycles at 200 mA g^{-1}. The 1D nanofiber assembly and hollow interior endow this material efficient contact with electrolyte, short Li$^+$ diffusion paths, and sufficient void spaces to accommodate large volume variation. The cost-efficient FeCO$_3$ with rationally designed nanostructures is a promising anode candidate for Li-ion batteries.


KEYWORDS: nanostructures, FeCO$_3$, anode materials, lithium-ion batteries, self-assembly
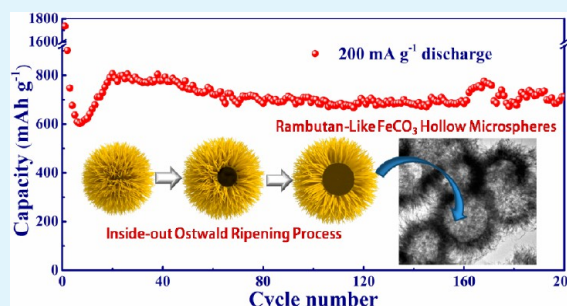
■ INTRODUCTION

Li-ion batteries (LIBs) are popular among the energy storage systems, because of their considerable merits, such as high energy density, long lifespan, and little memory effect. They cover various aspects in applications of electronics (such as laptops and mobile phones), and turn into a promising candidate for plug-in hybrid or all-electric vehicles and smart electric grids.[1,2] To satisfy the large-scale energy consumption, LIBs with higher capacity, as well as better cyclic stability and rate capability, attract massive consideration.[3,4] As one of the essential components in LIBs, the anode material is of significance to better performances. However, limited specific capacity and unsatisfactory high-rate performance of the commercial graphite-based materials are apparently far from the ever-increasing need for high-power applications. In this regard, numerous efforts have been made to explore advanced anode materials for next-generation LIBs.[5,6] Since Poizot et al.'s proposal,[7] various transition-metal oxides (TMOs, such as Fe$_3$O$_4$,[8−10] MnO,[11,12] and Co$_3$O$_4$[13,14]) and their analogues (transition-metal nitrides,[15] sulfides,[16] oxy-salts,[17,18] etc.) have been exploited, because of their high theoretical specific capacity, intrinsic safety, and natural abundance.[19]

As a new member in the family of conversion-type materials, transition-metal carbonates were also explored as LIB anode materials,[20] following the lithium storage mechanism:

$$MCO_3 + 2Li^+ + 2e^- \leftrightarrow M + Li_2CO_3$$

$$M = Fe, Co, Mn, ... \tag{1}$$
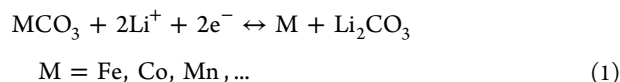
In addition to the merits of TMOs, these materials are also more cost-efficient and less time-consuming in synthesis, such as short hydrothermal time, low-temperature sintering, and one-step preparation without further treatment.[21−23] Tirado et al. first explored transition-metal carbonates as LIB anode materials, and as-prepared MnCO$_3$ submicrometer particles showed a reversible capacity of 460 mAh g^{-1} at 0.25 C,[22] and then they prepared modified pure and Co-substituted MnCO$_3$ materials through reverse micelle method, which exhibited higher cycling efficiency and better rate performance.[24] Also, Su et al. found that CoCO$_3$ submicrocube/graphene composites delivered a capacity over 1000 mAh g^{-1} with improved stability benefiting from the advantages of graphene.[25] These pioneer studies uncovered the potential of transition-metal carbonates as high-performance LIB anode materials.

Analogous to MnCO$_3$ and CoCO$_3$, FeCO$_3$, with a theoretical Li-storage capacity of ~462 mAh g^{-1}, which is also known as siderite that exists as a mineral in nature with abundant reserve. It is widely investigated in corrosion science and usually serves as precursor to acquire magnetite or hematite in materials science. Up to now, although many efforts have been made to fabricate FeCO$_3$ with unique morphologies, nanosized or microsized/nanosized structures were hardly achieved, because of the fast precipitation rate during preparation.[21,26−28] Meanwhile, these stuffed microstructures inevitably hinder the lithium storage performances, especially rate capability, because of their long Li-ion and electron diffusion paths as well as small electrode-electrolyte

contact area.[1,29] Apart from the poor ion transport kinetics above, these bulk materials also suffer from notable volume expansion and severe aggregation during conversion reactions, resulting in miserable cycling stability.[30−32] Herein, by utilizing economical urea as both soft template and carbonate source, we developed a facile hydrothermal route to prepare rambutan-like $FeCO_3$ hollow microspheres (HMSs) with a porous microscale/ nanoscale structure, and to the best of our knowledge, explored their lithium storage performances for the first time.

■ EXPERIMENTAL SECTION

Synthesis of $FeCO_3$ Hollow Microspheres (HMSs). Hierarchical $FeCO_3$ HMSs were synthesized via a facile hydrothermal method. In a typical preparation, 0.81 g $FeCl_3·6H_2O$ and 3.00 g urea were dissolved in 70 mL of distilled water, and then a homogeneous solution formed through magnetic agitation for 10 min. Next, 0.80 g of ascorbic acid was added to the above system under continuous agitation while the yellow liquid suddenly changed into a clear solution. After being stirred and sonically treated for 30 min, respectively, the transparent solution was transferred to a Teflon-lined stainless steel autoclave with 80 mL capacity, which was sealed and maintained at 160 °C for 3 h. The mixture was allowed to cool to room temperature naturally. The obtained brownish product was centrifuged and washed with distilled water and ethanol for at least three times separately, and then dried at 60 °C in an electric oven for further use.

Material Characterization. X-ray diffraction (XRD) measurements were operated on a Rigaku MiniFlex II diffractometer with Cu $K\alpha$ radiation (λ = 1.5418 Å). Morphology and structure were analyzed by field-emission scanning electron microscopy (FESEM, JEOL Model JSM-7500F), and transmission electron microscopy (TEM), and high-resolution transmission electron microscopy (HRTEM) (FEI Tecnai, Model G2F-20). The specific surface area and porosity were determined by N_2 adsorption/desorption isotherms through Micromeritics ASAP 2020 system.

Electrochemical Measurements. Electrochemical performances were evaluated in CR2025-type coin cells assembled in a high-purity argon-filled glove box with lithium as counter and reference electrodes. The working electrode was fabricated by mixing $FeCO_3$, conductive carbon black (Ketjen black) and poly(vinylidene fluoride) (PVDF) with the weight ratio of 75:15:10 to form slurry, and then coated onto copper foil. The mass of each electrode was 1.8 ± 0.2 mg. The electrolyte consists of a solution of 1 mol L^{-1} $LiPF_6$ in dimethyl carbonate (DMC), ethyl methyl carbonate (EMC), and ethylene carbonate (EC) (1:1:1 v/v/v). Celgard 2400 membrane was used as a separator. Discharge/charge tests were performed galvanostatically between the potential range of 0.01−3 V (vs Li/Li$^+$) under LAND-CT2001A battery testers. Cyclic voltammograms (CVs) were conducted on a Zahner-Elektrik IM6e electrochemical workstation recorded at a potential range of 0.01−3 V (vs. Li/Li$^+$). All the above measurements were conducted at room temperature.

■ RESULTS AND DISCUSSION

Structure and Morphology. The phase composition and purity of the as-prepared $FeCO_3$ was investigated by XRD. The well-defined XRD patterns shown in Figure 1 indicate a rhombohedral siderite $FeCO_3$ structure (space group: $R\overline{3}c$, JCPDS No. 29-696). It can be clearly distinguished that the diffraction peaks all correspond to each crystal plane.

The texture and morphology were characterized through FESEM and TEM. According to Figure 2a, the samples display morphologies of piled-up microspheres with diameters ranging from 2 μm to 4 μm. Closer observation (inset of Figure 2a) reveals that these microspheres exhibit hierarchical structures constituted by numerous nanofibers with the width of ∼70 nm. From a cracked microsphere in Figure 2b, the hollow interiors and the nanofiber subunits are clearly discerned. Similarly, in the TEM images (Figure 2d), we can distinctly identify hollow
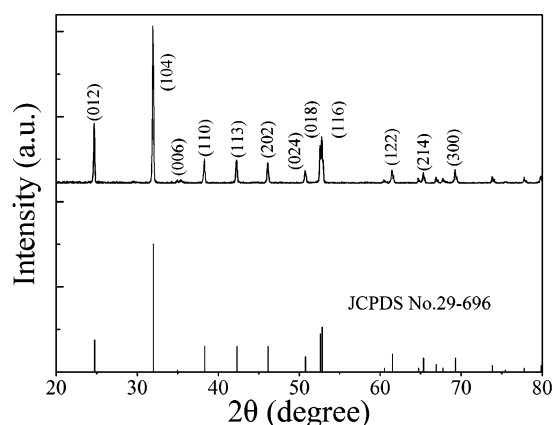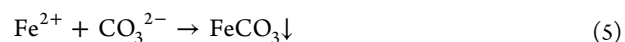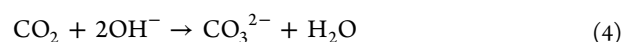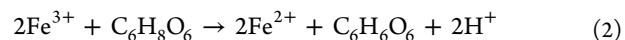

Figure 1. XRD patterns of $FeCO_3$ hollow microspheres (HMSs).

interiors and the outer shells through a marked contrast between the well-defined center and edge in the single microparticles. Moreover, lots of nanoscaled white vacancies are randomly distributed in the central region, suggesting the stacked porous constructions formed by primary nanofibers. Featuring at a close view, those dark-colored thin wires (indicated by arrows) can be identified as the fringes of the lamellar nanofibers, while the average thickness is as thin as 7.2 nm (depicted in Figure 2c). In addition, those nanofibers appear transparent, because of the high beam energy passing through, which further confirms these papery subunits. The (006) lattice spacing (0.254 nm) verifies the rhombohedral $FeCO_3$ crystal texture, as obviously observed in the representative HRTEM image (Figure 2e and 2f). As for porosity, the Brunauer−Emmett−Teller (BET) specific surface area of 30 m^2 g^{-1} was determined, and the average pore size was calculated as ∼14 nm (see Figure S1 in the Supporting Information). The mesopores arise from the piled nanofibers and microspheres, while the macropores can be attributed to the hollow spaces.

Through morphology and porosity observations, a unique porous structure with hollow interiors was discerned, and the large extra spaces may enhance the structural integrity by holding volume changes during continual discharge/charge cycles.[33] Also, one-dimensional (1D) structures together with nano-sized pores and hollow void facilitate a better contact with the electrolyte for high Li$^+$ flux across the interface.[34−36] These above favorable points guarantee this hierarchical $FeCO_3$ sample with outstanding electrochemical performances.

Formation Mechanism. According to the reactants, the formation of $FeCO_3$ can be described as the following formulas:

$$2Fe^{3+} + C_6H_8O_6 \rightarrow 2Fe^{2+} + C_6H_6O_6 + 2H^+ \tag{2}$$

$$CO(NH_2)_2 + 3H_2O \rightarrow 2NH_4^+ + CO_2 + 2OH^- \tag{3}$$

$$CO_2 + 2OH^- \rightarrow CO_3^{2-} + H_2O \tag{4}$$

$$Fe^{2+} + CO_3^{2-} \rightarrow FeCO_3\downarrow \tag{5}$$

Here, urea acts as the sources of carbonate and hydroxyl ions.[37] The former reacts with ferrous ion to form precipitates and the latter neutralizes hydrogen ions. We also studied the structure and morphology evolution of this hierarchical $FeCO_3$ sample by performing time-dependent experiments. The reactants start to deposit at ∼50 min, and only yellow suspension can be collected before that. It is worth mentioning that the interesting inside-out
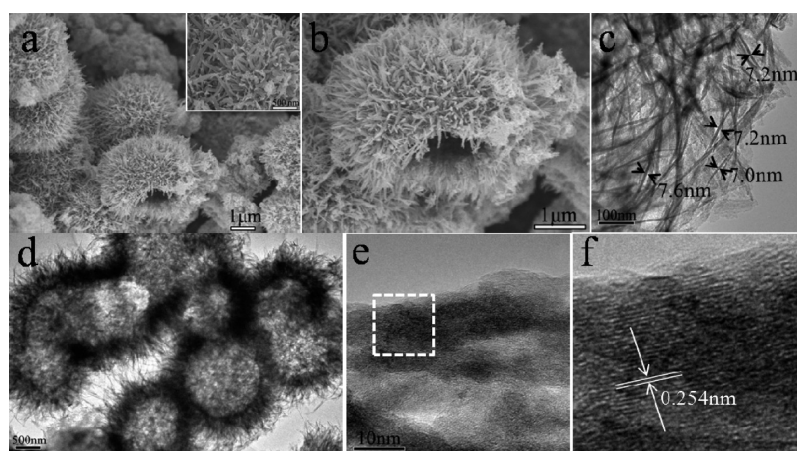
Figure 2. (a,b) Field-emission scanning electron microscopy (FESEM), (c,d) transmission electron microscopy (TEM), and (e,f) high-resolution transmission electron microscopy (HRTEM) images of as-prepared $FeCO_3$ HMSs. The highlighted region in panel (e) is shown in Panel (f).
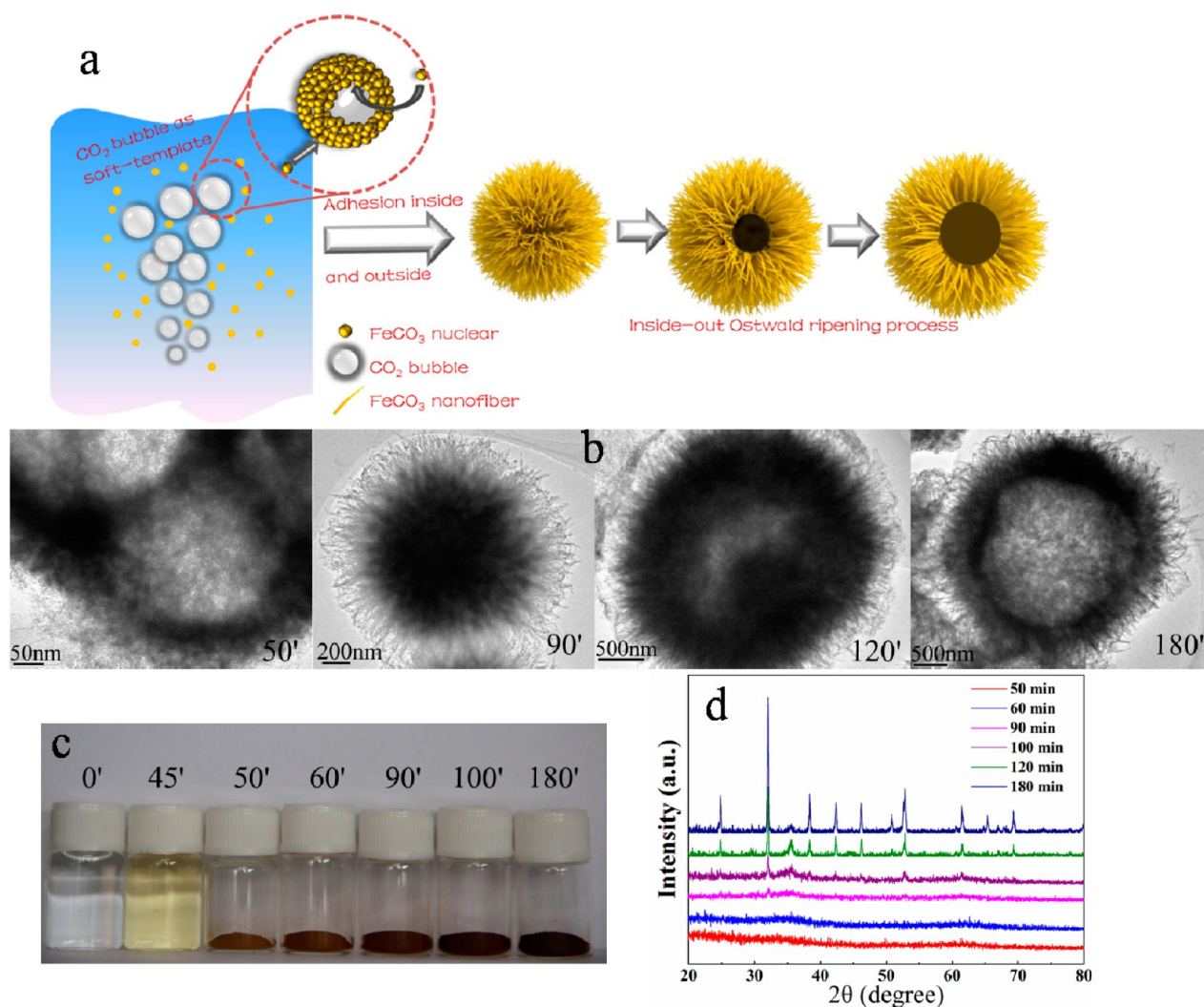

Figure 3. (a) Schematic illustration on the formation process of $FeCO_3$ hollow structures. Time-dependent variation on $FeCO_3$ microsphere, shown via (b) TEM images for a single particle, (c) colors by optical images, and (d) XRD patterns.

Ostwald ripening process plays a leading role of the formation of hollow interiors.[38]

Figure 3a illustrates visual description of this interesting ripening process with the growth of a single sphere, in which the augment of interior voids can be clearly identified. Firstly, numerous crystal nuclei self-assembled into a sub-micrometer hollow structure with the help of CO_2 bubbles as soft templates. Those constituted nanoparticles can be easily observed both in the TEM (Figure 3b) and SEM (see Figure S2 in the Supporting Information) images. Subsequently, the hollow interiors
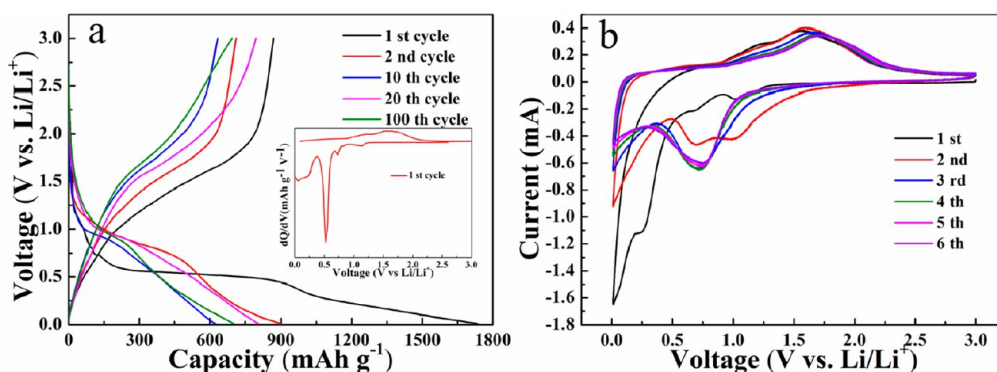
Figure 4. (a) Discharge−charge plots of different cycles at 200 mA g^{-1}, and the inset is differential capacity variation with voltages of the first cycle; (b) CV curves at a scan rate of 0.1 mV s^{-1} between 0.01 and 3 V vs Li/Li$^+$.
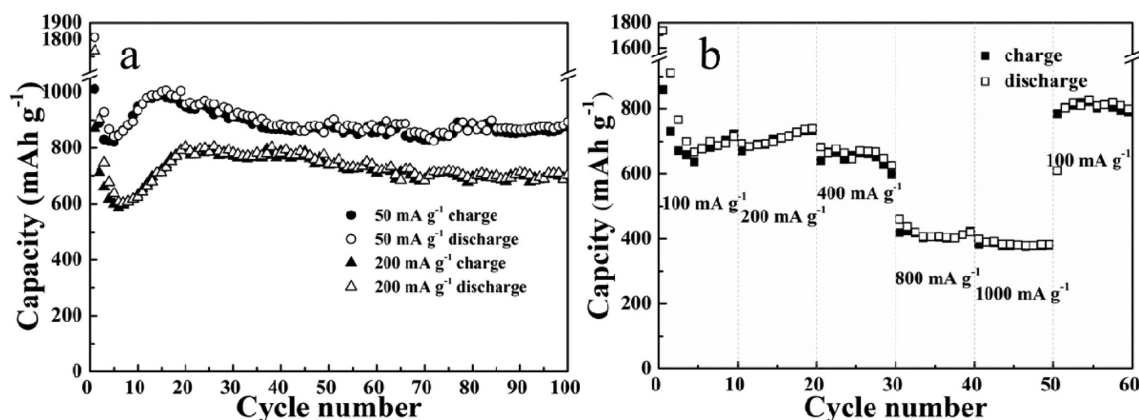

Figure 5. (a) Cycling performances of FeCO$_3$ HMSs at 50 mA g^{-1} and 200 mA g^{-1}; (b) rate capacity at different current densities. All galvanostatic tests were performed in the voltage range from 0.1 V to 3 V vs. Li/Li$^+$.

disappeared during the next period of 10 min (see Figure S3c in the Supporting Information). This may be ascribed to the fast growth of nuclei with burst of gas bubbles, which can be confirmed by the diameter increase and volume expansion of the sediments (see Figure S3 in the Supporting Information). After the formation of stuffed microspheres, the precipitates under-went a typical inside-out ripening process. Condensed particles turned into hollow structures, and a clear view of hollow effect can be identified (Figure 3b). The corresponding ex situ XRD and optical images also suggested this crystallization course. In addition to the color change from orange to claybank and then brown, the signal of diffraction peaks increased with prolonging reaction duration (see Figures 3c and 3d). From the amorphous nanoparticles to well-crystallized siderite, the ex situ XRD patterns display explicit structure evolution during Ostwald ripening. It is generally known that carbonate ions (CO$_3$$^{2-}$) have symmetrical and planar structures, which tend to form Fe−O octahedron between the different planes of CO$_3$$^{2-}$ during the formation of FeCO$_3$ nuclei (see Figure S4 in the Supporting Information). This character inclines to create lamellar morphology, thus ripening to a hierarchical construction during hydrothermal processes.[39]

Electrochemical Performances. Representative dis-charge−charge curves at 200 mA g^{-1} for various cycles are depicted in Figure 4a. During the initial cycle within a cut-off window of 0.01−3 V, high specific discharge and charge capacity of ∼1730 mAh g^{-1} and 925 mAh g^{-1} can be achieved. The irreversible capacity results from inevitable formation of solid electrolyte interface (SEI) film and extended electrolyte

degradation,[22] which is very common for most conversion electrode materials. The main plateau above 0.5 V, namely, the sharp peak centered at ∼0.52 V in the differential capacity versus potential curves (inset of Figure 4a), is attributed to the reduction of Fe^{2+} to metallic Fe^0 through typical conversion reactions.[18] Concerning cycling properties, the maximum of reversible capacity can reach above 800 mAh g^{-1} and remain stable at ∼700 mAh g^{-1}, according to the 20th cycle and 100th cycle, respectively. Obviously, the reversible capacity is much higher than the theoretical value, based on the conversion mechanism (eq 1). The origin of extra capacity may be ascribed to two parts: (i) the Faradaic contributions of side reactions with electrolyte and/or reversible formation of polymer/gel-like film through a so-called "pseudo-capacitance-type behavior";[40−42] and (ii) capacitive effects of the ultrafine porous structure of the hierarchical microspheres, also reported on metal oxysalts.[17,18]

Cyclic voltammograms were further conducted to investigate the electrochemical behaviors (Figure 4b). Initial cathodic scan reveals three main peaks at 1.03, 0.68, and 0.27 V, in agreement with the initial discharge curve. The first small peak is attributed to slight intercalation of Li$^+$ without structure changes, which coincides with many iron oxides.[43,44] The tiny peak at 0.68 V and broad peak below 0.5 V are the combination of complete reduction of Fe^{2+} to Fe, the formation of SEI film, and the electrolyte decomposition.[25,45] For the anodic scan, the humplike peaks at 1.27 and 1.56 V, and the succeeding broad anodic peaks centered at ∼1.65 V, are due to the oxidation of metallic Fe^0 to Fe^{3+}, similar to some Fe$_2$O$_3$-based materials.[18,43] The reduction peaks are replaced by a broad split peak shifting

11215

dx.doi.org/10.1021/am403453r | ACS Appl. Mater. Interfaces 2013, 5, 11212−11217

to ∼0.85 V with decreased intensity in the second cycle, indicating irreversible processes in the first cycle. Interestingly, the split peaks transform to one peak for the following cycle, which is ascribed to the amorphous nature/crystal structure destruction of the material, reported previously on some metal oxysalts and metal oxides.[46−48] Moreover, the subsequent CV curves overlap from the 3rd cycle to the 6th cycle, revealing good reversibility of Li storage performances.

Cyclic Stability. Cyclic performances were explored at the current density of 50 and 200 mA g^{-1}. As shown in Figure 5a, FeCO$_3$ HMSs provided high capacities of 880 and 700 mAh g^{-1} at 50 and 200 mA g^{-1}, respectively, suggesting the outstanding cyclic stability after 100 cycles. Note that the capacity increased to a similar value of the second cycle steadily (more than 1000 mAh g^{-1} at 50 mA g^{-1}) after a slope of decrease and maintained stable, as shown in the typical cyclic profile. Such an interesting phenomenon is commonly observed for many metal oxide and oxysalt materials,[18] which can be attributed to the existence of a possible activation procedure, along with the formation of the polymeric/gel-like film mentioned above.[19,49] Encouragingly, the calendar life can be extend to 200 cycles at a high current density of 200 mA g^{-1} with a stable capacity of 710 mAh g^{-1} in Figure 6, which is superior to metal oxysalts[24,46]
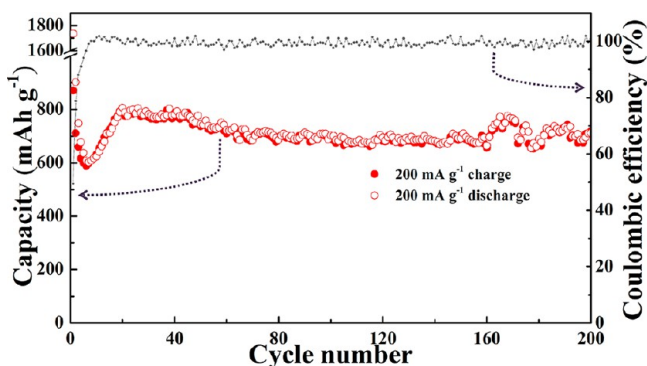

Figure 6. Long-term cyclic stability and coulombic efficiency of FeCO$_3$ HMSs at 200 mA g^{-1}.

and many pristine Fe-based MOs,[50,51] even comparable to some TMO/carbon composites.[52,53] In addition, the integrity of those structures could be preserved basically after many cycles (see Figure S5 in the Supporting Information).

In addition to cyclic ability, rate performance is another key point for practical application as high-power anode electrodes. Benefiting from the porous structure and hollow interiors with shorter Li$^+$ diffusion path, FeCO$_3$ HMSs reveal excellent cyclic response to continuously increasing current densities. As demonstrated in Figure 5b, after an incline of activation process, the capacity steadily increased to 722 mAh g^{-1} at 200 mA g^{-1} and remained steady for the next repeated discharge−charge sequences. Significantly, even working at a high rate of 1000 mAh g^{-1}, a satisfactory capacity over 380 mAh g^{-1} can be obtained and maintain level. When the measurements are reversed to 100 mA g^{-1}, the specific capacities can fully recover to original values, demonstrating a stable cyclic capacity of more than 800 mAh g^{-1}.

Such remarkable lithium storage performance, especially high specific capacity with enhanced cyclic stability and favorable rate ability, should be referred to the architectural merits of these hollow spheres. As mentioned above, the hollow structure along with 1D nanofibers can bring about short Li$^+$ diffusion path and ample contact with the electrolyte, leading to efficient ion

transport. Moreover, the stacked subunits form porous constructions with hollow interiors, and consequently improve the structural integrity during the repeated discharge/charge processes by moderating the mechanical strain induced by volume change. These features assure sufficient utilization of active materials during cycling, and effectively alleviate the pulverization of electrode aroused by conversion reactions, hence enhancing the lithium storage performances.

CONCLUSION

In summary, we have fabricated the hierarchically rambutan-like FeCO$_3$ HMSs assembled by nanofiber building blocks via a facile one-step hydrothermal method. The primary submicrometer spheres undergo an interesting inside-out hollowing process with the growth of 1D subunits, and form a perspective porous structure. Benefiting from these unique structural features, the as-synthesized FeCO$_3$ HMSs demonstrate superior rate capability and cyclic performance, with long-term stable capacity of ∼710 mAh g^{-1} for 200 cycles. Combining major merits of Fe-based materials, this class of functional materials will definitely possess bright prospects in developing advanced materials for the next-generation LIBs through rational and delicate design. The real origin of the high extra capacity in FeCO$_3$ HMSs should be deeply explored through extensive experiments.

ASSOCIATED CONTENT

ⓢ Supporting Information

SEM, TEM, and optical images of intermediate products, structural illustration, N$_2$ adsorption−desorption isotherm, and pore size distribution of FeCO$_3$ HMSs, and SEM images of FeCO$_3$ HMSs after cycles. This material is available free of charge via the Internet at http://pubs.acs.org.

AUTHOR INFORMATION

Corresponding Author
*E-mail: zhouzhen@nankai.edu.cn.

Notes
The authors declare no competing financial interest.

NOTE ADDED IN PROOF

When checking the proof, we notice a new report on CoCO$_3$-polypyrrole composites as Li ion battery anodes. The authors confirmed the participation of reversible reactions between C(IV) in CO$_3^{2-}$ and low-valence carbon for Li storage,[54] which was firstly proposed in our previous work,[25] and has been supported by our recent report.[55] These results also assist in explaining the origin of the high Li storage capacity in FeCO$_3$, yet more investigations are highly desired to thoroughly clarify detailed electrochemical reactions of transition metal carbonates with Li.

ACKNOWLEDGMENTS

REFERENCES

(1) Bruce, P. G.; Scrosati, B.; Tarascon, J. M. *Angew. Chem., Int. Ed.* **2008**, *47*, 2930−2946.
(2) Cheng, F.; Tao, Z.; Liang, J.; Chen, J. *Chem. Mater.* **2008**, *20*, 667−681.
(3) Li, H.; Wang, Z.; Chen, L.; Huang, X. *Adv. Mater.* **2009**, *21*, 4593−4607.

(4) Wang, Y.; Li, H.; He, P.; Hosono, E.; Zhou, H. *Nanoscale* **2010**, *2*, 1294−1305.

(5) Jiang, J.; Li, Y.; Liu, J.; Huang, X. *Nanoscale* **2011**, *3*, 45−58.

(6) Su, L.; Jing, Y.; Zhou, Z. *Nanoscale* **2011**, *3*, 3967−3983.

(7) Poizot, P.; Laruelle, S.; Grugeon, S.; Dupont, L.; Tarascon, J. M. *Nature* **2000**, *407*, 496−499.

(8) Chen, J. S.; Zhang, Y.; Lou, X. W. *ACS Appl. Mater. Interfaces* **2011**, *3*, 3276−3279.

(9) Yuan, S. M.; Li, J. X.; Yang, L. T.; Su, L. W.; Liu, L.; Zhou, Z. *ACS Appl. Mater. Interfaces* **2011**, *3*, 705−709.

(10) Xu, J. S.; Zhu, Y. J. *ACS Appl. Mater. Interfaces* **2012**, *4*, 4752−4757.

(11) Su, L.; Zhong, Y.; Wei, J.; Zhou, Z. *RSC Adv.* **2013**, *3*, 9035−9041.

(12) Xu, G. L.; Xu, Y. F.; Fang, J. C.; Fu, F.; Sun, H.; Huang, L.; Yang, S.; Sun, S. G. *ACS Appl. Mater. Interfaces* **2013**, *5*, 6316−6323.

(13) Xiao, X.; Liu, X.; Zhao, H.; Chen, D.; Liu, F.; Xiang, J.; Hu, Z.; Li, Y. *Adv. Mater.* **2012**, *24*, 5762−5766.

(14) Xu, G. L.; Li, J. T.; Huang, L.; Lin, W.; Sun, S.-G. *Nano Energy* **2013**, *2*, 394−402.

(15) Gillot, F.; Oró-Solé, J.; Palacín, M. R. *J. Mater. Chem.* **2011**, *21*, 9997−10002.

(16) Seo, J. W.; Jang, J. T.; Park, S. W.; Kim, C.; Park, B.; Cheon, J. *Adv. Mater.* **2008**, *20*, 4269−4273.

(17) Aragón, M. a. J.; León, B.; Pérez Vicente, C.; Tirado, J. L.; Chadwick, A. V.; Berko, A.; Beh, S.-Y. *Chem. Mater.* **2009**, *21*, 1834−1840.

(18) Ang, W. A.; Gupta, N.; Prasanth, R.; Madhavi, S. *ACS Appl. Mater. Interfaces* **2012**, *4*, 7011−7019.

(19) Lei, C.; Han, F.; Li, D.; Li, W. C.; Sun, Q.; Zhang, X. Q.; Lu, A. H. *Nanoscale* **2013**, *5*, 1168−1175.

(20) Reddy, M. V.; Subba Rao, G. V.; Chowdari, B. V. *Chem. Rev.* **2013**, *113*, 5364−5457.

(21) Xuan, S.; Chen, M.; Hao, L.; Jiang, W.; Gong, X.; Hu, Y.; Chen, Z. *J. Magn. Magn. Mater.* **2008**, *320*, 164−170.

(22) Aragón, M. J.; León, B.; Pérez Vicente, C.; Tirado, J. L. *J. Power Sources* **2011**, *196*, 2863−2866.

(23) Yuan, J.; Zhu, J.; Bi, H.; Zhang, Z.; Chen, S.; Liang, S.; Wang, X. *RSC Adv.* **2013**, *3*, 4400−4407.

(24) Mirhashemihaghighi, S.; Leon, B.; Perez Vicente, C.; Tirado, J. L.; Stoyanova, R.; Yoncheva, M.; Zhecheva, E.; Saez Puche, R.; Arroyo, E. M.; Romero de Paz, J. *Inorg. Chem.* **2012**, *51*, 5554−5560.

(25) Su, L.; Zhou, Z.; Qin, X.; Tang, Q.; Wu, D.; Shen, P. *Nano Energy* **2013**, *2*, 276−282.

(26) Chirita, M.; Ieta, A. *Cryst. Growth Des.* **2012**, *12*, 883−886.

(27) Liu, X.; Wang, H.; Su, C.; Zhang, P.; Bai, J. *J. Colloid Interface Sci.* **2010**, *351*, 427−432.

(28) Xuan, S.; Hao, L.; Jiang, W.; Song, L.; Hu, Y.; Chen, Z.; Fei, L.; Li, T. *Cryst. Growth Des.* **2007**, *7*, 430−434.

(29) Arico, A. S.; Bruce, P.; Scrosati, B.; Tarascon, J. M.; Van Schalkwijk, W. *Nat. Mater.* **2005**, *4*, 366−377.

(30) Guo, J.; Liu, Q.; Wang, C.; Zachariah, M. R. *Adv. Funct. Mater.* **2012**, *22*, 803−811.

(31) Kang, E.; Jung, Y. S.; Cavanagh, A. S.; Kim, G. H.; George, S. M.; Dillon, A. C.; Kim, J. K.; Lee, J. *Adv. Funct. Mater.* **2011**, *21*, 2430−2438.

(32) Li, X.; Wang, C. *J. Mater. Chem. A* **2013**, *1*, 165−182.

(33) Wang, X.; Wu, X. L.; Guo, Y. G.; Zhong, Y.; Cao, X.; Ma, Y.; Yao, J. *Adv. Funct. Mater.* **2010**, *20*, 1680−1686.

(34) Wang, Z.; Zhou, L.; David Lou, X. W. *Adv. Mater.* **2012**, *24*, 1903−1911.

(35) Vu, A.; Qian, Y.; Stein, A. *Adv. Energy Mater.* **2012**, *2*, 1056−1085.

(36) Li, X.; Dhanabalan, A.; Wang, C. *J. Power Sources* **2011**, *196*, 9625−9630.

(37) Xiong, S.; Chen, J. S.; Lou, X. W.; Zeng, H. C. *Adv. Funct. Mater.* **2012**, *22*, 861−871.

(38) Liu, B.; Zeng, H. C. *Small* **2005**, *1*, 566−571.

(39) Liu, G.; Deng, Q.; Wang, H.; Ng, D. H. L.; Kong, M.; Cai, W.; Wang, G. *J. Mater. Chem.* **2012**, *22*, 9704−9713.

(40) Su, L.; Zhou, Z.; Shen, P. *J. Phys. Chem. C* **2012**, *116*, 23974−23980.

(41) Laruelle, S.; Grugeon, S.; Poizot, P.; Dollé, M.; Dupont, L.; Tarascon, J. M. *J. Electrochem. Soc.* **2002**, *149*, A627−A634.

(42) Su, L.; Zhou, Z.; Shen, P. *Electrochim. Acta* **2013**, *87*, 180−185.

(43) Chen, S.; Bao, P.; Wang, G. *Nano Energy* **2013**, *2*, 425−434.

(44) Jain, G.; Balasubramanian, M.; Xu, J. J. *Chem. Mater.* **2006**, *18*, 423−434.

(45) Sun, Y.; Hu, X.; Luo, W.; Xia, F.; Huang, Y. *Adv. Funct. Mater.* **2013**, *23*, 2436−2444.

(46) Aragon, M. J.; Leon, B.; Perez Vicente, C.; Tirado, J. L. *Inorg. Chem.* **2008**, *47*, 10366−10371.

(47) Cherian, C. T.; Reddy, M. V.; Rao, G. V. S.; Sow, C. H.; Chowdari, B. V. R. *J. Solid State Electrochem.* **2012**, *16*, 1823−1832.

(48) Cherian, C. T.; Sundaramurthy, J.; Kalaivani, M.; Ragupathy, P.; Kumar, P. S.; Thavasi, V.; Reddy, M. V.; Sow, C. H.; Mhaisalkar, S. G.; Ramakrishna, S.; Chowdari, B. V. R. *J. Mater. Chem.* **2012**, *22*, 12198−12204.

(49) Wang, Z.; Luan, D.; Madhavi, S.; Hu, Y.; Lou, X. W. *Energy Environ. Sci.* **2012**, *5*, 5252−5256.

(50) Liu, J.; Li, Y.; Fan, H.; Zhu, Z.; Jiang, J.; Ding, R.; Hu, Y.; Huang, X. *Chem. Mater.* **2010**, *22*, 212−217.

(51) Lee, G. H.; Park, J. G.; Sung, Y. M.; Chung, K. Y.; Cho, W. I.; Kim, D. W. *Nanotechnology* **2009**, *20*, 295205−295209.

(52) Muraliganth, T.; Vadivel Murugan, A.; Manthiram, A. *Chem. Commun.* **2009**, 7360−7362.

(53) Ma, J.; Yu, F.; Wen, Z.; Yang, M.; Zhou, H.; Li, C.; Jin, L.; Zhou, L.; Chen, L.; Yuan, Z.; Chen, J. *Dalton Trans.* **2013**, *42*, 1356−1359.

(54) Ding, Z. J.; Yao, B.; Feng, J. K.; Zhang, J. X. *J. Mater. Chem. A* **2013**, *1*, 11200−11209.

(55) Su, L. W.; Zhong, Y. R.; Zhou, Z. *J. Mater. Chem. A* **2013**, DOI: 10.1039/C3TA13233A.